

Hurricane Imaging Radiometer (HIRAD) Wind Speed Retrievals and Validation Using Dropsondes

Daniel J. Cecil¹ and Sayak K. Biswas²

¹ NASA Marshall Space Flight Center, Huntsville, AL

² Universities Space Research Association, Huntsville, AL

Journal of Atmospheric and Oceanic Technology

Corresponding author email: Daniel.J.Cecil@nasa.gov

17

Abstract

18 Surface wind speed retrievals have been generated and evaluated using Hurricane
19 Imaging Radiometer (HIRAD) measurements from flights over Hurricane Joaquin, Hurricane
20 Patricia, Hurricane Marty, and the remnants of Tropical Storm Erika, all in 2015. Procedures are
21 described here for producing maps of brightness temperature, which are subsequently used for
22 retrievals of surface wind speed and rain rate across a ~50 km wide swath for each flight leg. An
23 iterative retrieval approach has been developed to take advantage of HIRAD's measurement
24 characteristics. Validation of the wind speed retrievals has been conducted, using 636
25 dropsondes released from the same WB-57 high altitude aircraft carrying HIRAD during the
26 Tropical Cyclone Intensity (TCI) experiment.

27 The HIRAD wind speed retrievals exhibit very small bias relative to the dropsondes, for
28 winds tropical storm strength (17.5 m s^{-1}) or greater. HIRAD has reduced sensitivity to winds
29 weaker than tropical storm strength, and a small positive bias ($\sim 2 \text{ m s}^{-1}$) there. Two flights with
30 predominantly weak winds according to the dropsondes have abnormally large errors from
31 HIRAD, and large positive biases. From the other flights, root mean square differences between
32 HIRAD and the dropsonde winds are 4.1 m s^{-1} (33%) for winds below tropical storm strength,
33 5.6 m s^{-1} (25%) for tropical storm strength winds, and 6.3 m s^{-1} (16%) for hurricane strength
34 winds. Mean absolute differences for those categories are 3.2 m s^{-1} (25%), 4.3 m s^{-1} (19%), and
35 4.8 m s^{-1} (12%), with bias near zero for tropical storm and hurricane strength winds.

36

37 **1. Introduction**

38 Mapping the surface wind speed in a hurricane is a great challenge that affects the ability
39 to issue accurate forecasts and warnings for the maximum wind speed, wind field structure, and
40 related impacts (Powell et al. 2009; Uhlhorn and Nolan 2012; Nolan et al. 2014). Buoys can
41 provide useful measurements, but only for the precise parts of a hurricane that happen to track
42 across the buoy. As with any surface stations, buoys are subject to failures in extreme conditions
43 (i.e., the high winds and large waves of a hurricane). Satellite-based instruments typically are
44 limited in heavy rain or very high wind speed conditions, or have coarse spatial resolution.
45 Dropsondes from reconnaissance or research aircraft can provide detailed vertical profiles of the
46 wind, but are necessarily limited in their coverage. The Stepped Frequency Microwave
47 Radiometers (SFMR) on hurricane hunter aircraft are very good at estimating surface wind speed
48 in hurricane conditions, but only along a nadir trace directly beneath the aircraft (Uhlhorn and
49 Black 2003; Uhlhorn et al. 2007; Klotz and Uhlhorn 2014).

50 The Hurricane Imaging Radiometer (HIRAD) is an experimental four-channel, C-band,
51 synthetic thinned array radiometer designed to *map* ocean surface wind speeds in hurricanes.
52 Wind speed retrievals from HIRAD take advantage of the fact that the C-band emissivity of the
53 ocean surface increases with increasing foam coverage, which results from wave breaking
54 ([Nordberg et al. 1971](#); [Rosenkranz and Staelin 1972](#)). Since the increase in foam is correlated
55 with surface wind speed ([Ross and Cardone 1974](#); [Webster et al. 1976](#); [Swift et al. 1984](#); [Tanner
56 et al. 1987](#)), emissivity increases with surface wind speed. The sensitivity to wind speed is
57 greatest at hurricane-force ($> 33 \text{ m s}^{-1}$) and is therefore particularly useful for measuring the
58 strongest winds. The four C-band channels also have varying sensitivity to rain, so rain rate and
59 wind speed can be retrieved simultaneously. This concept is similar to that employed by the

60 SFMR. Interferometric signal processing enables construction of a cross-track swath from
61 HIRAD, such that the instrument functions as a pushbroom imager without mechanical scanning.

62 HIRAD has been flown on high-altitude aircraft (\sim 20 km) in order to map \sim 50 km wide
63 swaths from individual flight legs across hurricanes. In 2015, it overflew Atlantic Hurricane
64 Joaquin, the remnants of Tropical Storm Erika, and Eastern North Pacific Hurricanes Patricia
65 and Marty as part of the Office of Naval Research Tropical Cyclone Intensity (TCI) project
66 (Doyle et al. 2017). Data processing methods and the production of wind speed retrievals from
67 those flights are discussed in Sections 2 and 3. TCI also featured the High Definition Sounding
68 System (HDSS) (Black et al. 2016), with dropsonde spacing sometimes less than 10 km.
69 Quantitative comparison of HIRAD wind speed retrievals with near-surface wind speeds
70 measured by dropsondes are discussed in Section 4.

71

72 **2. HIRAD data processing and scene construction**

73

74 a) Scene construction and calibration

75 In HIRAD there are ten antenna elements connected to ten dedicated receivers. Each of
76 the antenna elements has a long, thin (fan beam) antenna pattern (Bailey et al. 2010) oriented in
77 the cross-track direction relative to the heading of the platform. All ten fan beams overlap,
78 defining a brightness temperature strip to be imaged. The pixels along the strip are resolved
79 using synthetic antenna beams generated by interferometric techniques (Ruf et al. 1988).
80 Forward motion of the platform creates a pushbroom imager, with a cross-track strip of data
81 recorded approximately every second. This cross-track strip will be referred to as a scan, and the

82 individual synthetic beam positions within the scan referred to as "scan positions". Nominal
83 measurement characteristics are listed in Table 1.

84 The basic measurement of HIRAD is called a visibility vector, which consists of cross
85 correlations (visibilities) of signals from all possible pairs of ten antenna elements. This includes
86 the self-correlation, or zeroth visibility. The cross-track scene is reconstructed from those cross
87 correlations. The zeroth visibility (or "Antenna Temperature" in traditional radiometry
88 nomenclature) is a measurement of the average brightness temperature of the cross-track scene
89 weighted by the fan-beam antenna power pattern. The non-zero visibilities (cross-correlation
90 between two *different* antenna elements) provide measurements of the perturbation of the scene
91 about the mean (zeroth visibility). Depending on the spacing between pairs of correlating
92 antenna elements, components of this perturbation with different spatial frequencies are sampled.
93 The cross-track scene is reconstructed by combining the average value and the perturbations at
94 36 different spatial frequencies (similar to a Fourier reconstruction). The highest resolution
95 possible for the image is determined by the highest spatial frequency sampled – which
96 corresponds to the maximum possible distance between any two antenna elements in the HIRAD
97 array.

98 Various types of error affect the image reconstruction procedure (Swift et al. 1991). The
99 brightness temperature error for a given pixel in the cross-track scene can result from systematic
100 offsets in the data and from random, zero-mean, measurement noise. The random component is
101 a characteristic of the particular instrument design and is easily predicted. The systematic biases
102 are harder to predict since they typically result from an incomplete or incorrect accounting of the
103 sources of offset and gain corrections when calibrating the instrument. Temperature variations
104 across the antenna are a major contributor to this. Although termed "systematic", they are not

105 necessarily constant throughout a flight, or repeatable from one flight to the next. As the
106 temperature variations evolve, so do these systematic errors.

107 For HIRAD, the systematic errors are much greater in magnitude than the random errors.
108 Design considerations have been identified that could greatly reduce those errors in the future,
109 but data from the current experimental version of the instrument require substantial post-
110 processing to reduce artifacts resulting from those errors.

111 The initial scene construction follows standard techniques for synthetic thinned array
112 radiometers (Tanner and Swift 1993). The visibility vector is multiplied by the “Moore-Penrose
113 pseudoinverse” (Penrose 1955) of the instrument’s impulse response matrix (termed the “G
114 matrix”). This G matrix was previously derived from measurements in an anechoic chamber and
115 its pseudo inverse (Gp) was computed based on techniques discussed by Tanner and Swift
116 (1993) and Goodberlet (2000). The cross track brightness temperature distribution obtained
117 from the multiplication of Gp and V exhibits ripples as discussed by Ruf (1991). A combined
118 effect of truncation of the lower visibility spectrum due to the antenna pattern envelope on the
119 zeroth visibility interference pattern and inconsistencies between the different antenna element
120 patterns produce these ripples. These ripples, along with the effect of synthetic antenna beam
121 patterns, are compensated to produce a “true” brightness temperature image using a linear
122 correction (antenna pattern correction) per pixel. The antenna pattern correction is derived from
123 measurements of well-characterized hot and cold target scenes. A blackbody absorber during a
124 pre-deployment calibration is used for the hot scene. For the cold target scenes, we use
125 precipitation-free sections of flight legs over the ocean, selecting regions where winds are
126 expected to be relatively weak and homogeneous. Multiple cold target scenes are selected for
127 each flight, so the antenna pattern correction evolves during the flight to account for small

128 calibration drifts. To characterize the cold target, a radiative transfer model is applied to an
129 assumed surface state and atmospheric profile. The same radiative transfer model is used for the
130 wind speed retrieval discussed in section 3. The sea surface temperature is taken from the Multi-
131 scale Ultra-high Resolution Sea Surface Temperature (<https://mur.jpl.nasa.gov>). Surface wind
132 speeds for the cold calibration targets are taken from dropsondes, with wind speeds less than 7 m
133 s⁻¹. A fixed atmospheric profile of temperature, water vapor, and cloud liquid water is taken
134 from idealized numerical simulations of hurricanes described by Amarin et al. (2012). At
135 HIRAD's C-band frequencies, sensitivity to realistic variations in these atmospheric profiles is
136 small (Smith 1982; Tsang et al. 1977) compared to the instrument's measurement error. The
137 scene construction and brightness temperature calibration is conducted separately for each of
138 HIRAD's four frequencies.

139 HIRAD was built as a first prototype of an experimental instrument, to demonstrate the
140 feasibility of a wide-swath, airborne, hurricane wind speed sensor. Non-ideal characteristics of
141 its novel multi-frequency array antenna, a varying thermal environment during flight, and
142 possibly an interaction with the aircraft radome combine to produce data with artificial along-
143 track streaks where brightness temperatures are biased high or low. The magnitude of those
144 streaks varies between channels, from flight to flight, and also within flight. This lack of
145 consistency for the streaks makes them particularly difficult to objectively correct or remove.
146 Some improvements in our initial scene construction procedure have made the streaks less
147 prominent in the 2015 TCI HIRAD data than in data collected during previous field campaigns.
148 The HIRAD measurement system includes some redundancies in zeroth and non-zero visibility
149 measurements, and the radiometer passband for each frequency channel is divided into multiple
150 subbands. Using optimal combinations of subbands and redundant visibilities does produce

151 somewhat “cleaner” initial scenes. Of the ten HIRAD antenna elements, inconsistencies in the
152 zeroth visibility time series were found associated with antenna 1, 6, 8, 9, and 10. Non-zero
153 visibilities associated with those antennae are now preferentially rejected before image
154 reconstruction, when redundant baselines involving other antennae are available. For each flight,
155 subbands are now selected based on their consistency across all four frequencies. Earlier data
156 from HIRAD’s 4.0 GHz channel had been so dominated by streaks, that it previously appeared
157 useless. With the improvements implemented for the 2015 TCI dataset, the 4.0 GHz channel is
158 now incorporated in wind speed retrievals for the first time.

159

160 b) Smoothing and filtering

161 HIRAD was designed to sense only horizontally polarized (H-pol) emission from the
162 target scene. Since the H-pol emissivity of the ocean surface decreases with increasing incidence
163 angle, HIRAD’s brightness temperature images are generally brightest near the nadir direction
164 and the intensity decreases gradually away from nadir. This effect overwhelms the counter
165 effect of a small increase due to longer atmospheric slant path for the pixels away from nadir.
166 (The atmospheric contribution to measured brightness temperature is minimal at these C-band
167 frequencies (Smith et al. 1982; Tsang et al. 1977).) The geophysical signature resulting from
168 wind and rain gets modified by this systematic variation of cross track brightness temperature.
169 As an attempt to compensate for this effect, an expected brightness temperature swath is
170 computed using the radiative transfer model for a hypothetical clear, calm ocean scene with zero
171 wind speed and no rain. This background scene is expected to have only the crosstrack
172 variations that result from instrument viewing geometry for a specular ocean surface. The
173 background scene is subtracted from the measured scene to produce an array of “excess

174 brightness temperatures" (Fig. 1), which *should* not have any systematic cross-track variability
175 except that due to variability in the actual underlying scene. In the measured data, these excess
176 brightness temperatures do exhibit cross-track variability due to the streaks mentioned in the
177 previous subsection.

178 An ad hoc filtering was developed that treats each flight leg and each frequency
179 separately. For each cross-track scan position (0 on the left, 320 on the right), the mean value of
180 excess brightness temperature is computed for the entire flight leg. Then the fractional relative
181 bias is computed for each scan position. This is the bias for a given scan position, divided by the
182 mean excess brightness temperature of the other scan positions. Because HIRAD measurements
183 carry the least uncertainty near the center of the swath, this bias is computed relative to the mean
184 of the innermost 107 (out of 321 total) scan positions (that is, the innermost $\pm 19^\circ$). Each scan
185 position is then assigned a weight, inversely proportional to the absolute value of the fractional
186 relative bias. Streaks (scan positions with systematically high or low biases) are thus given little
187 weight in the subsequent smoothing. Scan positions with little bias would have weight
188 approaching infinity, but for practical application the weight is limited to a value of 10 (Fig. 2a).

189 The weighting based on each scan position's relative bias is then combined with a
190 Gaussian spatial smoothing using 41 pixels (± 20 left and right) in the cross-track direction (Fig.
191 2b). A stronger spatial smoothing is applied for the 4.0 and 5.0 GHz channels than for the 6.0
192 and 6.6 GHz channels, because the lower frequency channels tend to have a greater number of
193 prominent streaks in the initial data, with smaller spacing between those streaks. The stronger
194 smoothing essentially allows the filter to look further away from a given scan position to find
195 relatively good (low biased, heavily weighted) data to include in the solution.

196 Consider scan position 130 in Fig. 2, which is 10.6° left (southwest) of the center of the
197 flight track in Fig. 1. Here the value for the 4.0 GHz weighting function is 0.84 in Fig. 2a, one of
198 the smallest values anywhere, because this scan position corresponds to a prominent streak in Fig.
199 1a. For scan position 130 in Fig. 2b (the top strip, for 4.0 GHz), neighboring pixels about 10-20
200 scan positions to the left and 10-20 scan positions to the right contribute more to the smoothed,
201 filtered excess brightness temperature than scan positions very near 130 do. For scan position
202 195, on the other hand, the opposite is true. The weighting function in Fig. 2a maxes out at 10.0,
203 so pixels very near scan position 195 contribute most to the smoothed, filtered solution there.

204 For the 6.6 GHz channel, the bias-related weighting function is near 10.0 (red line in Fig.
205 2a) for most of the swath, indicating that most of the streaks are low amplitude and do not need
206 much correction. The spatial Gaussian filter then dominates the solution in the bottom strip of
207 Fig. 2b. The main exception for 6.6 GHz is around scan position 37, viewing 49° left of the
208 center of the flight track, where a prominent positive bias can be seen in Fig. 1d.

209 This smoothing is applied to instrument data that are strongly over-sampled relative to
210 horizontal resolution (Table 1). The spacing between measurements is only a few hundred
211 meters, but the footprint size (i.e., the size of a synthetic antenna beam) for those measurements
212 is a few km in each direction. Because the raw data are so strongly oversampled, the effective
213 footprint size after smoothing is only slightly larger than before smoothing, except near the edges
214 of the swath (Table 1 and Fig. 3).

215 The effect of the smoothing is demonstrated by comparing the initial excess brightness
216 temperatures (Fig. 1) to the filtered, smoothed excess brightness temperatures (Fig. 4). The
217 background brightness temperature that was originally subtracted is ultimately added back to the

218 filtered, smoothed excess brightness temperatures. This yields the final quality controlled
219 brightness temperatures that are used for wind speed and rain rate retrievals.

220

221 **3. Retrieval approach**

222 Our preferred retrieval approach is to construct simultaneous maximum likelihood
223 estimates (MLE) of surface wind speed and column-averaged rain rate. This can be done by
224 minimizing the difference between a vector of measured brightness temperatures at HIRAD's
225 four frequencies, and a vector of modeled brightness temperatures from an ensemble of possible
226 wind / rain combinations (Amarin et al. 2011). The treatment of surface emissivity as a function
227 of wind speed follows the model of El-Nimri et al. (2010). The microwave absorption by rain
228 follows Klotz and Uhlhorn (2014), using their Equation 12 and the revised coefficients listed in
229 their Table 3. The surface emissivity and rain absorption models are consistent with the
230 operational algorithm for the SFMR (Klotz and Uhlhorn 2014). The surface emissivity model
231 also factors in incidence angle and polarization effects for HIRAD (El-Nimri et al. 2010). Since
232 the surface emissivity models used for SFMR and HIRAD are based in part on estimates of 1-
233 minute mean wind speed derived from dropsondes, the retrieved winds can be interpreted as 1-
234 minute mean estimates. There is considerable uncertainty in what scales are truly being resolved
235 by any of these radiometer or dropsonde measurements. Morris and Ruf (2015) additionally
236 describe accounting for HIRAD's slant path view through an inhomogeneous rain field. The
237 complication of *varying* rain along the slant path is not accounted for in the retrievals presented
238 here, but it may be incorporated with future algorithm improvements. The length of the slant
239 path through the rain layer is accounted for, after assuming that liquid rain extends 5 km in the
240 vertical.

241 Ice particles are neglected in the radiative transfer model, as emission is negligible at
242 these frequencies and scattering should be negligible in all but the rarest of cases. If ice
243 scattering does occur, it would preferentially reduce brightness temperatures in the higher
244 frequency channels, which would be misinterpreted as a reduction in rain rate. The best
245 observational assessment we can make for potential ice scattering effects involves the Advanced
246 Microwave Precipitation Radiometer (AMPR), which has flown on the NASA ER-2 with
247 comparable altitudes and comparable spatial resolution as HIRAD on the WB-57. Cecil et al.
248 (2010) mentioned that a slight scattering signature could even be seen in AMPR's lowest
249 frequency (10.7 GHz) channel upon close inspection of data from Hurricane Emily (2005).
250 Given that HIRAD's highest frequency channel has >60% longer wavelength (4.5 cm, versus 2.8
251 cm for AMPR's 10.7 GHz channel) we doubt that HIRAD would have been compromised by ice
252 scattering. That Hurricane Emily case is thought to have the most intense convection of any
253 hurricane case documented using high-altitude (~20 km) aircraft (Cecil et al. 2010; Heymsfield
254 et al. 2010). Leppert and Cecil (2015) did show 10.7 GHz ice scattering reducing the AMPR
255 brightness temperatures up to about 40 K in Oklahoma severe thunderstorms. HIRAD's
256 frequencies could conceivably be useful for identifying large hail in severe thunderstorms, but
257 comparable conditions are exceedingly rare in hurricanes.

258 Conceptually, the retrieval should account for strong winds generating foam on the sea
259 surface and raising the brightness temperatures in all C-band frequencies, and absorption /
260 emission by liquid rain drops preferentially raising the brightness temperatures in the higher
261 frequency channels. Looking at the smoothed, filtered excess brightness temperatures in Fig. 4,
262 one would expect most of the flight leg to have substantial surface wind, because brightness
263 temperatures are elevated in all four channels. The quasi-circular eyewall near the southeast end

264 of the leg likely has a combination of very strong wind and heavy rain, with elevated brightness
265 temperatures in all channels and a greater enhancement in the highest frequencies. A more linear
266 band (oriented from southwest to northeast) near the far southeast end of the flight leg is likely
267 dominated by heavy rain, with its signal much stronger in the high frequency channels than the
268 lower frequency channels.

269 Morris and Ruf (2015) showed rain rate retrievals from HIRAD, but noted that wind
270 speed retrievals are more problematic because of sensitivity to the calibration. In our initial
271 attempts to simultaneously retrieve wind speed and rain rate, the solutions are especially
272 sensitive to relative calibration differences between the highest and lowest frequency channels
273 used. If the 4.0 GHz channel is biased low relative to the 6.6 GHz channel, the retrieval will
274 interpret this as a scene with mostly rain and little wind. The opposite is true if the 4.0 GHz
275 channel is biased high, relative to the 6.6 GHz channel. The same pattern holds true if any
276 combination of two, three, or four channels is used for the retrieval, with the solution being
277 dominated by the relative differences between highest and lowest frequency channels.

278 The streaks discussed in Section 2, and imperfections in their removal, lead to patterns of
279 relative calibration biases when comparing two or more channels. As such, the initial retrievals
280 tend to alternate in unrealistic ways between interpreting a signal as being from very heavy rain
281 with little wind, or very strong wind with no rain. The result can be a checkerboard pattern. A
282 constrained MLE approach (Linwood Jones, personal communication, 2016) in which values for
283 one scan are only allowed to change by some reasonable amount from the previous scan helps
284 alleviate the problem of unrealistically alternating between light and strong wind.

285 Since more elegant retrieval approaches are not effective with the noisy measurements,
286 we developed an iterative approach that combines simpler individual retrievals. Basically we

287 conduct a sequence of single-channel retrievals, with the results from one retrieval constraining
288 the possible solutions from the next retrieval.

289

- 290 • First, we run single-channel MLE retrievals for each channel, constraining the
291 wind speed at a given scan position to change by no more than 1.5 m s^{-1} from one
292 scan to the next. The 1.5 m s^{-1} value is somewhat arbitrary, but allows a realistic
293 limit on the wind speed gradient ($7.5 \text{ m s}^{-1} \text{ km}^{-1}$ in the along-track direction) in the
294 initial retrievals. The resulting wind speeds subjectively look credible (but
295 probably biased a bit low) from the 4.0 GHz and 5.0 GHz retrievals. Wind speed
296 retrievals from 6.0 GHz and 6.6 GHz subjectively look biased too low, with too
297 much retrieved rain.
- 298 • Second, for each pixel we take the maximum value of the wind speed retrievals
299 from 4.0 GHz and 5.0 GHz, calling this MaxWS45. We then re-run the single
300 channel retrievals separately for 6.0 and 6.6 GHz, but constrain those retrievals to
301 use MaxWS45 as the minimum possible wind speed solution for a given pixel.
302 This allows the higher frequency channels to refine the wind speed estimate, and
303 with their better effective spatial resolution they can refine the horizontal wind
304 speed map.
- 305 • Third, for each pixel we take the mean of the 6.0 and 6.6 GHz wind speed
306 retrievals, calling this MeanWS67.
- 307 • Fourth, the final wind speed product for each pixel (FinalWS) is computed as the
308 mean of MaxWS45 and MeanWS67.
- 309 • Finally, we re-run a retrieval of rain rate only, providing that retrieval with
FinalWS and the 6.6 GHz brightness temperature as inputs. This yields a rain rate

310 pattern that takes advantage of the channel with the most responsiveness to rain,
311 but is physically consistent with the wind speed that was derived from the
312 previous steps.

313 This iterative approach is certainly not the most elegant, and we do not necessarily
314 recommend using it for other instruments or for future data from HIRAD after improvements to
315 the instrument hardware are made. It is a novel approach that provides useful maps of hurricane
316 wind speed from the imperfect data that have already been collected.

317

318 **4. Comparison with dropsondes**

319 Retrieved HIRAD wind speeds (Cecil et al. 2016) were compared with near surface wind
320 speed estimates from 636 HDSS dropsondes (Bell et al. 2016) in TCI flights over Hurricane
321 Joaquin (2015), Hurricane Marty (2015), Hurricane Patricia (2015), and the remnants of Tropical
322 Storm Erika (2015). Some of the flights over Marty and Patricia were at the tropical storm stage,
323 with subsequent flights at hurricane stage. Doyle et al. (2017) summarize the TCI flights and
324 datasets. From the quality controlled dropsonde wind profiles, a layer-average wind speed is
325 computed over the lowest 150 m of the profile (WL150), or the lowest 500 m (MBL, for mean
326 boundary layer) if low level data are unavailable (Franklin et al. 2003). This averaging removes
327 some of the effect of gustiness in the dropsonde wind profile. Near surface wind speed is
328 estimated from WL150 using the coefficients in Uhlhorn et al.'s (2007) Fig. 2. Otherwise it is
329 estimated as 80% of the MBL value, following Franklin et al. (2003). Comparisons were made
330 using any dropsonde that supported such a surface wind estimate, with its lowest reported
331 location within the +/-60° swath from HIRAD.

332 For comparisons between HIRAD and dropsonde winds, the HIRAD wind speed
333 retrievals are averaged over 500-m radius from the lowest reported location of the dropsonde.
334 We have not accounted for storm motion in these comparisons. The dropsonde takes about 10-
335 15 minutes to reach the surface, after being released from nearly 20 km altitude. The tropical
336 cyclone itself could translate several km during that time, with smaller scale features translating
337 further if moving near the speed of local winds. Some of the largest differences between the
338 HIRAD and dropsonde wind estimates appear to result from these storm motion effects, coupled
339 with tight gradients of wind speed near the eyewall.

340 Scatterplots of HIRAD versus dropsonde wind speed estimates are stratified by flight
341 (Fig. 5a) and incidence angle (Fig. 5b) in order to check for any obvious, consistent biases.
342 HIRAD retrievals from the Hurricane Patricia 21 October flight do appear high biased, with
343 several points having $25-45 \text{ m s}^{-1}$ retrieved by HIRAD where the dropsondes indicate less than
344 20 m s^{-1} winds. The flight over the remnants of Tropical Storm Erika also had substantial high
345 bias (the blue points toward the lower-left of Fig. 5a), which was expected because HIRAD has
346 low sensitivity to weak wind speeds. Our retrievals artificially set a minimum wind speed at 10 m s^{-1} ,
347 because of this known low sensitivity to weak winds. Data from the other flights are
348 generally scattered within 20% of the one-to-one line, other than outliers at low wind speeds
349 (especially where dropsondes indicate $< 20 \text{ m s}^{-1}$ wind). Other than the Patricia 21 October
350 flight, the largest differences are associated with drops in the eye of Hurricane Patricia on 23
351 October and Hurricane Joaquin on 4 October, with retrieved wind speeds around 40 m s^{-1} and
352 dropsonde wind speeds $< 20 \text{ m s}^{-1}$. These dropsondes splashed where HIRAD depicts a strong
353 gradient between the eye and eyewall. Two of these are seen in the northern part of the
354 eye/eyewall interface region in Fig. 6a. Based on 7 m s^{-1} storm motion from Hurricane Patricia's

355 best track, the eye may have translated about 5 km further north-northeast while the sondes were
356 falling. That would place these sondes (and similarly, the sonde from Hurricane Joaquin on 4
357 October) in the low-wind center mapped by HIRAD. The retrieved winds there are still too
358 strong, likely because of the sea surface being roughened in this small eye itself, and because
359 HIRAD has little sensitivity below about 15 m s^{-1} .

360 Although the purpose of this paper is to document the wind speed retrievals, the
361 corresponding rain rate retrieval for the 23 October Hurricane Patricia flight is also mapped in
362 Fig. 6c. For perspective, an 89-GHz satellite image is included in Fig. 6d. We suspect the rain
363 retrievals are effective at distinguishing between moderate and heavier rain rates, but have not
364 performed a quantitative evaluation. In this particular case, the retrieved rain rates have maxima
365 in the northwest and southeast portions of the eyewall, immediately upwind and downwind of
366 the retrieved wind speed maximum on the southwestern side. The retrieval could be assigning
367 too much rain and not enough wind in the locations of the rain maxima, too much wind and not
368 enough rain in the location of the wind maximum, or some combination of the two. The extreme
369 wind speeds retrieved by HIRAD near 2100 UTC 23 October (76 m s^{-1}) are plausible, given best
370 track estimates of 180 kt (93 m s^{-1}) at 1800 UTC and 130 kt (67 m s^{-1}) during landfall at 2300
371 UTC. The nadir-viewing SFMR on a NOAA P3 aircraft retrieved 67 m s^{-1} in the southeastern
372 quadrant at 2033 UTC, with its flight track offset about 10 km from the portion of the swath with
373 HIRAD's peak winds (Rogers et al. 2017).

374 Statistics from the HIRAD versus dropsonde comparisons are listed separately for each
375 flight in Table 2. As described above, the flights over Tropical Storm Patricia on 21 October and
376 the remnants of Tropical Storm Erika on 30 August have larger differences and much larger
377 biases than the other flights. Most flights had small positive biases (less than 2 m s^{-1}), with root

378 mean square differences around 6 m s^{-1} and mean absolute differences around 4 m s^{-1} . The
379 biases are smallest over the range of tropical storm strength wind speeds (Table 3). The
380 differences are largest in magnitude where HIRAD indicates hurricane strength winds, but the
381 percentage difference is smallest for hurricane strength winds and largest for wind speeds weaker
382 than tropical storm strength. Excluding the two problematic flights brings the bias below 2 m s^{-1}
383 for all ranges of wind speed, and reduces the other error statistics noticeably. Further excluding
384 the three eye dropsondes that were described above, where large differences are probably related
385 to storm motion while the dropsondes fall, virtually eliminates the bias associated with hurricane
386 strength wind speeds (Table 4). That also reduces the root mean square difference (mean
387 absolute difference) for the remaining sample to 5.0 m s^{-1} (3.8 m s^{-1}), and for hurricane strength
388 winds reduces those differences to 6.3 m s^{-1} (4.8 m s^{-1}).

389 No bias related to incidence angle is apparent in Fig. 5b. The high wind speeds in this
390 comparison are mostly at high incidence angles, and low wind speeds at low incidence angles.
391 But that is a result of high wind speeds carrying the dropsondes far to the side of the flight track,
392 where HIRAD views with a high incidence angle. The few data points with a high wind speed
393 retrieved at low incidence angle, or low wind speed at high incidence angle, do fall near the one-
394 to-one line.

395

396 **5. Summary, Discussion, and Future Directions**

397 Data processing, smoothing / filtering, and surface wind speed retrieval techniques are
398 described here for data collected by HIRAD in the 2015 TCI field experiment. Validation of the
399 wind speed retrievals is presented using nearly coincident measurements from 636 dropsondes.
400 HIRAD is an experimental instrument that maps scenes of C-band microwave brightness

401 temperatures, with about 50 km swath width when flown around 20 km altitude. Surface wind
402 speed is derived from those brightness temperatures, based on relationships between surface
403 wind speed, resulting foam coverage on the ocean surface, and ocean surface microwave
404 emissivity. HIRAD's four frequencies between 4.0 and 6.6 GHz are used to account for
405 microwave emissions from liquid rain while retrieving surface wind speed.

406 Imperfections in the initial measurements must be accounted for in order to produce
407 useful wind speed retrievals. Smoothing and filtering techniques described in Section 2b are
408 designed to rely most on those parts of the measurements that exhibit the least noise for a given
409 flight leg. An iterative wind speed retrieval technique described in Section 3 then uses the two
410 lower frequency channels (4.0 and 5.0 GHz) to generate a first guess wind field. This constrains
411 subsequent retrievals using the higher frequency (6.0 and 6.6 GHz) channels that provide more
412 spatial detail. This approach is a compromise between more elegant approaches used with the
413 operational, nadir-viewing SFMR (Klotz and Uhlhorn 2014), and practical considerations
414 associated with experimental instrumentation.

415 The comparison between HIRAD- and dropsonde-derived surface wind speeds is quite
416 encouraging. Flights over two of the weakest systems had abnormally large errors – the 30
417 August flight over the remnants of Tropical Storm Erika, and the 21 October flight over Tropical
418 Storm Patricia. The current HIRAD antenna has low sensitivity to wind speeds below about 15
419 m s^{-1} , so confidence was low for those flights anyway. The HIRAD retrievals have a small
420 positive bias ($\sim 2 \text{ m s}^{-1}$) at wind speeds less than tropical storm strength (17 m s^{-1}), in part
421 because the retrieval artificially assumes at least 10 m s^{-1} wind everywhere.

422 Excluding the two aforementioned flights with abnormally large errors, and three
423 dropsondes where the comparisons are especially compromised by storm motion during

424 dropsonde descent, HIRAD's bias is near zero for tropical storm and hurricane strength winds.
425 The root mean square difference between HIRAD- and dropsonde-estimated wind speed is
426 around 5 m s^{-1} , and the mean absolute difference is around 4 m s^{-1} . Those values are higher in
427 magnitude for hurricane strength winds (about 6 and 5 m s^{-1} , respectively), but in percentage
428 terms the differences are lowest for hurricane strength winds (16% root mean square difference,
429 12 % mean absolute difference).

430 The validation of HIRAD wind speed retrievals has been presented here in terms of
431 differences relative to dropsonde-based estimates, as distinct from being true error estimates.
432 The root mean square difference in the HIRAD-versus-dropsonde comparisons results from
433 HIRAD measurement and retrieval errors themselves, errors in the estimation of surface wind
434 speed from the dropsondes, and the inherent variability of the true wind field. We consulted
435 Nolan et al.'s (2013) Hurricane Nature Run and a simulation of a smaller, more intense storm
436 provided by D. Nolan (Fig. 7) to estimate that spatiotemporal variability in the true wind field
437 contributes $\sim 2\text{-}3 \text{ m s}^{-1}$ uncertainty to such comparisons. For uncertainty from the dropsonde-
438 based surface wind speed estimates, we consider the 3.1 m s^{-1} root mean square difference
439 reported in Fig. 3 of Uhlhorn et al. (2007). Using these values together with the 6.0 m s^{-1} root
440 mean square difference in the HIRAD – dropsonde comparisons gives a rough estimate of root
441 mean square error as $\text{RMSE}_{\text{HIRAD}} = ((6.0 \text{ m s}^{-1})^2 - (3.1 \text{ m s}^{-1})^2 - (2 \text{ m s}^{-1})^2)^{0.5} = 4.7 \text{ m s}^{-1}$. Just as
442 our HIRAD – dropsonde comparisons had differences exceeding 20 m s^{-1} in a few cases along
443 the eyewall wind speed gradient, the simulation in Fig. 7d also has some differences exceeding
444 $\pm 20 \text{ m s}^{-1}$ in similar locations. While the largest differences relate to motion of the eye itself
445 during the time it takes a dropsonde to descend, Fig. 7d also shows many locations where
446 differences of a few m s^{-1} likely result from features rotating through the cyclonic flow. Merely

447 removing a vortex-scale motion would not account for the cyclonic translation of smaller scale
448 features. In practice, removing vortex-scale motion of a real hurricane is also difficult because
449 short time scale “wobbles” of the eye are not captured by the best track.

450 The operational SFMR and its wind speed retrieval algorithm are considered the state of
451 the art for this type of remote sensing, although the SFMR only measures a trace at nadir instead
452 of mapping across a swath. The SFMR has been flown in hurricanes since 1980, with multiple
453 generations of designs, hardware, and retrieval algorithms (Uhlhorn and Black 2003 and
454 references therein; Uhlhorn et al. 2007; Klotz and Uhlhorn 2014). Klotz and Uhlhorn (2014)
455 reported on the SFMR algorithm versions that were operational from 2006-2014 (termed
456 “operational” in that paper), and the current version that became operational in 2015 (termed
457 “revised” in that paper). The newer version reduced the SFMR bias for wind speeds below
458 hurricane strength from $2\text{-}3 \text{ m s}^{-1}$ to $0\text{-}1 \text{ m s}^{-1}$. Biases for hurricane strength winds were near
459 zero for both versions. Root mean square difference versus dropsondes was reduced from 4.5 m
460 s^{-1} (2006 version) to 3.9 m s^{-1} (2015 version), computed over the full range of wind speeds.
461 Considering the SFMR’s long history of frequent hurricane flights, HIRAD’s relative youth (first
462 flown in 2010, with flights over seven hurricanes through 2015), and the challenge of mapping a
463 wide swath of winds, HIRAD’s performance as documented here is promising.

464 Efforts are currently underway to improve HIRAD’s measurement capabilities. A new
465 antenna design has been tested, indicating that improved sensitivity to lower wind speeds can be
466 achieved. Improvements to the integrated antenna – beamformer system, and to the thermal
467 control, should reduce the raw measurement errors that currently necessitate a complicated
468 retrieval approach. Even with the measurements that have already been collected, better
469 retrievals might be achieved with certain modifications to our current approach. The spatial

470 smoothing that is currently applied may be stronger than is necessary. Our MLE retrievals
471 initially consider all possible combinations of wind speed and rain rate; historical SFMR
472 retrievals or output from high resolution numerical models could be used to constrain which
473 combinations of wind speed and rain rate are more likely to occur in nature.

474 Most of the interesting cases with data collected by HIRAD have been flown with the
475 NASA WB-57 high altitude aircraft. Besides the flights used here from the 2015 TCI field
476 experiment, there were three flights over Hurricane Gonzalo (2014) and one flight each over
477 Hurricane Earl (2010) and Hurricane Karl (2010). The data processing and retrieval approaches
478 described here could be applied to data from those flights, although there were no dropsonde-
479 derived surface wind estimates for validation. In the future, flights on a high altitude, long
480 endurance Global Hawk could conceivably provide wide swaths of wind speed (similar to those
481 from WB-57) but with several repeated (or rotated) passes during a single mission. Alternatively,
482 flights with HIRAD mounted on a lower altitude (~3 km) WP-3D aircraft would provide finer
483 spatial resolution over a smaller swath width (~7 km). Instrumentation normally flown on the
484 NOAA WP-3D during hurricanes would be suitable for addressing HIRAD's calibration and
485 validation, improving the characterization of rain in the retrievals, and connecting the surface
486 wind speed field with the wind field aloft as derived from Doppler radar.

487

488 *Acknowledgments*

489 This work was supported by the Office of Naval Research Tropical Cyclone Intensity experiment,
490 under MIPR N0001416IP00056. W. Linwood Jones and his group at the University of Central
491 Florida Remote Sensing Laboratory contributed to retrieval algorithm development. We thank
492 the crew of the NASA WB-57 and the rest of the TCI experiment team for their efforts in

493 collecting this data, particularly Mark Beaubien, Lee Harrison, and Michael Bell for their
494 collection and quality control of the HDSS dropsonde data. We thank Chris Ruf and two
495 anonymous reviewers for helpful comments on previous versions of this manuscript, and Dave
496 Nolan for providing the Hurricane Nature Run and additional model output. HIRAD and HDSS
497 data from the TCI experiment are available from NCAR's Earth Observing Laboratory. HIRAD
498 data from this and other experiments are available from NASA Marshall Space Flight Center's
499 Global Hydrology Resource Center. Sea Surface Temperatures used as inputs to our calibration
500 and retrievals were obtained from the Jet Propulsion Laboratory Multi-scale Ultra-high
501 Resolution Sea Surface Temperature (<https://mur.jpl.nasa.gov>).

502

503

504 **References**

505 Amarin, R.A., W.L. Jones, S.F. El-Nimri, J.W. Johnson, C.S. Ruf, T.L. Miller, and E. Uhlhorn,
506 2012. Hurricane wind speed measurements in rainy conditions using the airborne
507 Hurricane Imaging Radiometer (HIRAD). *IEEE Transactions on Geoscience and Remote
508 Sensing*, **50**(1), pp.180-192.

509 Bailey, M. C., R. Amarin, J. Johnson, P. Nelson, M. James, D. Sikmons, C. Ruf, L. Jones and X.
510 Gong, 2010: Multi-Frequency Synthetic Thinned Array Antenna for the Hurricane
511 Imaging Radiometer. *IEEE Trans. Ant. & Prop.*, **58**, 2562-2570.

512 Bell, M.M., J.D. Doyle, M. Beaubien, T. Allen, B.R. Brown, J. Dunion, P. Duran, J. Feldmeier,
513 L.C. Harrison, E. Hendricks, W. Jeffries, W. Komaromi, J. Martinez, J. Molinari, J.
514 Moskaitis, D.P. Stern, and D. Vollaro, 2016: ONR Tropical Cyclone Intensity 2015
515 NASA WB-57 HDSS Dropsonde Data. Version 1.0. UCAR/NCAR - Earth Observing
516 Laboratory. <https://doi.org/10.5065/D6KW5D8M>. Accessed 12 Apr 2016.

517 Black, P., L. Harrison, M. Beaubien, R. Bluth, R. Woods, A. Penny, R. Smith, and J. Doyle,
518 2016: High Definition Sounding System (HDSS) for atmospheric profiling. *J. Atmos.
519 Oceanic Technol.* doi:10.1175/JTECH-D-14-00210.1, in press.

520 Cecil, D. J., K. R. Quinlan, and D. M. Mach, 2010: Intense convection observed by NASA ER-2
521 in Hurricane Emily (2005). *Mon. Wea. Rev.*, **138**, 765-780.

522 Cecil, D.J., S.K. Biswas, W.L. Jones, and F. Alquaied, 2016: Hurricane Imaging Radiometer
523 (HIRAD) Data. Version 2.1. UCAR/NCAR - Earth Observing Laboratory.
524 <https://doi.org/10.5065/D6CF9NGC>. Accessed 4 Nov 2016.

525 Doyle, J.D. and 32 others, 2017: A View of Tropical Cyclones from Above: The Tropical
526 Cyclone Intensity (TCI) Experiment. *Bull. Amer. Meteor. Soc.*, *early online release*,
527 <http://dx.doi.org/10.1175/BAMS-D-16-0055.1>.

528 El-Nimri, S.F., W.L. Jones, E. Uhlhorn, C. Ruf, J. Johnson and P. Black, 2010: An Improved C-
529 Band Ocean Surface Emissivity Model at Hurricane-Force Wind Speeds Over a Wide
530 Range of Earth Incidence Angles. *IEEE Geosci. Rem. Sens. Letters*, **7**, 641-645.

531 Franklin, J. L., M. L. Black, and K. Valde, 2003: GPS dropwindsonde wind profiles in
532 hurricanes and their operational implications. *Wea. Forecasting*, **18**, 32–44.

533 Goodberlet, M.A., 2000: Improved image reconstruction techniques for synthetic aperture
534 radiometers. *IEEE Trans. Geosci. Rem. Sens.*, **38**, 1362-1366.

535 Heymsfield, G.M., L. Tian, A.J. Heymsfield, L. Li, and S. Guimond, 2010: Characteristics of
536 deep tropical and subtropical convection from nadir-viewing high-altitude airborne
537 Doppler radar. *J. Atmos. Sci.*, **67**, 285-308.

538 Klotz, B.W. and E.W. Uhlhorn, 2014: Improved stepped frequency radiometer tropical cyclone
539 surface winds in heavy precipitation. *J. Atmos. Oceanic Technol.*, **31**, 2392-2408.

540 Leppert II, K.D., and D.J. Cecil, 2015: Signatures of hydrometeor species from airborne passive
541 microwave data for frequencies 10-183 GHz. *J. Appl. Meteor. Clim.*, **54**, 1313-1334.

542 Morris, M. and C.S. Ruf, 2015: A Coupled-Pixel Model (CPM) atmospheric retrieval algorithm
543 for high-resolution imagers. *J. Atmos. Oceanic Technol.*, **32**, 1866-1879.

544 Nolan, D. S., R. Atlas, K. T. Bhatia, and L. R. Bucci (2013), Development and validation of a
545 hurricane nature run using the joint OSSE nature run and the WRF model. *J. Adv. Model.
546 Earth Syst.*, **5**, 382–405, doi:[10.1002/jame.20031](https://doi.org/10.1002/jame.20031).

547 Nolan, D.S., J.A. Zhang, and E.W. Uhlhorn, 2014: On the limits of estimating the maximum
548 wind speeds in hurricanes. *Mon. Wea. Rev.*, **142**, 2814-2837.

549 Nordberg, W. J., J. Conaway, D. B. Ross, and T. Wilheit, 1971: Measurements of microwave
550 emission from a foam-covered, wind-driven sea. *J. Atmos. Sci.*, **28**, 429–435,

551 Penrose, R., 1955: A generalized inverse for matrices. *Mathematical Proceedings of the
552 Cambridge Philosophical Society*, 51(3), pp. 406–413. doi: 10.1017/S0305004100030401.

553 Powell, M.D., E.W. Uhlhorn, and J.D. Kepert, 2009: Estimating maximum surface winds from
554 hurricane reconnaissance measurements. *Wea. Forecasting*, **24**, 868-883.

555 Rogers, R.F., S. Aberson, M.M. Bell, D.J. Cecil, J.D. Doyle, J. Morgerman, L.K. Shay, and C.
556 Velden, 2017: Re-writing the tropical record books: The extraordinary intensification of
557 Hurricane Patricia (2015). *Bull. Amer. Meteor. Soc.*, early online release. DOI:
558 <http://dx.doi.org/10.1175/BAMS-D-16-0039.1>

559 Rosenkranz, P. W., and D. H. Staelin, 1972: Microwave emissivity of ocean foam and its effect
560 on nadiral radiometric measurements. *J. Geophys. Res.*, **77**, 6528–6538

561 Ross, D. B., and V. Cardone, 1974: Observations of oceanic whitecaps and their relation to
562 remote measurements of surface wind speed. *J. Geophys. Res.*, **79**, 444–452.

563 Ruf, C.S., 1991: Error analysis of image reconstruction by a synthetic aperture interferometric
564 radiometer. *Radio Sci.*, **26**, 1419-1434.

565 Ruf, C. S., C. T. Swift, A. B. Tanner, and D. M. Le Vine, 1988: Interferometric synthetic
566 aperture microwave radiometry for the remote sensing of the earth. *IEEE Trans. Geosci.
567 Remote Sens.*, **26**, 5, 597-611.

568 Smith, E. K., 1982: Centimeter and millimeter wave attenuation and brightness temperature due
569 to atmospheric oxygen and water vapor. *Radio Sci.*, **17**, 1455–1464.

570 Swift, C. T., D. C. DeHorty, P. G. Black, and J.-Z. Chein, 1984: Microwave remote sensing of
571 ocean surface wind speed and rain rates over tropical storms. *Frontiers of Remote*
572 *Sensing of the Oceans and Troposphere from Air and Space Platforms: Proceedings of*
573 *the URSI Commission F Symposium and Workshop*, NASA Conference Publication, Vol.
574 2303, NASA, 281–286.

575 Swift, C.T., D.M. LeVine, C.S. Ruf, 1991: Aperture synthesis concepts in microwave remote
576 sensing of the earth. *IEEE Transactions on Microwave Theory and Techniques*, **39.12**,
577 1931-1935.

578 Tanner, A. C., C. T. Swift, and P. G. Black, 1987: Operational airborne remote sensing of wind
579 speeds in hurricanes. *Preprints, 17th Conf. on Hurricanes and Tropical*
580 *Meteorology*, Miami, FL, Amer. Meteor. Soc., 385–387.

581 Tanner, A.B. and C. T. Swift, 1993: Calibration of a synthetic aperture radiometer. *IEEE Trans.*
582 *Geosci. Rem. Sens.*, **31**, 257-267.

583 Tsang, L., J. A. Kong, E. Njoku, D. H. Staelin, and J. W. Waters, 1977: Theory for microwave
584 thermal emission from a layer of cloud or rain. *IEEE Trans. Antennas Propag.*, **25**, 650–
585 657.

586 Uhlhorn, E.W. and P.G. Black, 2003: Verification of remotely sensed sea surface winds in
587 hurricanes. *J. Atmos. Oceanic Technol.*, **20**, 99–116, doi:10.1175/MWR-D-11-00073.1.

588 Uhlhorn, E.W., P. G. Black, J. L. Franklin, M. Goodberlet, J. Carswell, and A. S. Goldstein,
589 2007: Hurricane surface wind measurements from an operational Stepped Frequency
590 Microwave Radiometer. *Mon. Wea. Rev.*, **135**, 3070–3085, doi:10.1175/MWR3454.1.

591 Uhlhorn, E.W. and D. S. Nolan, 2012: Observational undersampling in tropical cyclones and
592 implications for estimated intensity. *Mon. Wea. Rev.*, **140**, 825–840, doi:10.1175/MWR-
593 D-11-00073.1.

594 Webster, W. J., Jr., T. T. Wilheit, D. B. Ross, and P. Gloersen, 1976: Spectral characteristics of
595 the microwave emission from a wind-driven foam-covered sea. *J. Geophys.
596 Res.*, **81**, 3095–3099,

597

598

599 Table 1. HIRAD measurement characteristics from a nominal 20 km altitude and 200 m s^{-1}
 600 forward motion, roughly consistent with WB-57 flights.

		Near nadir	40° off nadir	50° off nadir	55° off nadir
Swath width		-	33.6 km	47.7 km	57.1 km
Across-track sampling		0.1 km	0.2 km	0.4 km	0.6 km
Along-track sampling		0.2 km	0.2 km	0.2 km	0.2 km
Measurement footprint size (km x km)	4.0 GHz:	1.6 x 2.5	3.6 x 4.3	6.1 x 6.1	8.2 x 7.7
	5.0 GHz:	1.6 x 2.0	3.6 x 3.4	6.1 x 4.9	8.2 x 6.1
	6.0 GHz:	1.6 x 1.7	3.6 x 3.0	6.1 x 4.2	8.2 x 5.3
	6.6 GHz:	1.6 x 1.7	3.6 x 2.9	6.1 x 4.1	8.2 x 5.2
Effective footprint size <i>after</i> <i>smoothing</i> (km x km)	4.0 GHz:	1.6 x 2.5	3.8 x 4.5	7.2 x 6.8	11.3 x 9.3
	5.0 GHz:	1.6 x 2.0	3.7 x 3.5	6.3 x 5.0	9.6 x 6.6
	6.0 GHz:	1.6 x 1.7	3.7 x 3.0	6.5 x 4.4	9.1 x 5.6
	6.6 GHz:	1.6 x 1.7	3.6 x 2.9	6.6 x 4.3	10.0 x 5.8

601

602 Table 2. Sample size, bias, root mean square difference, and mean absolute difference for
603 HIRAD comparisons with dropsondes, stratified by flights.

Flight	Sample size	Bias (m s ⁻¹)		RMSD (m s ⁻¹)		MAD (m s ⁻¹)	
Post-Erika 30 Aug	46	5.7	47%	6.7	54%	5.7	47%
TS Marty 27 Sep	50	2.0	13%	4.4	28%	3.8	24%
Hurricane Marty 28 Sep	68	1.7	8%	5.8	28%	4.4	22%
Hurricane Joaquin 02 Oct	73	1.6	12%	5.7	30%	4.2	23%
Hurricane Joaquin 03 Oct	64	-0.1	2%	5.8	34%	4.7	26%
Hurricane Joaquin 04 Oct	73	0.0	2%	5.8	29%	4.0	21%
Hurricane Joaquin 05 Oct	65	2.5	17%	4.2	30%	3.1	20%
TS Patricia 21 Oct	57	5.5	21%	9.4	36%	6.5	28%
Hurricane Patricia 22 Oct	71	0.0	0%	4.4	23%	3.4	18%
Hurricane Patricia 23 Oct	69	-0.4	-3%	6.7	23%	4.1	17%
<i>All</i>	636	1.6	11%	6.0	31%	4.3	24%
<i>Excluding 30 Aug, 21 Oct</i>	533	0.9	6%	5.4	28%	4.0	21%

604

605

606 Table 3. As in Table 2, but stratified by HIRAD wind speeds below tropical storm (TS) strength,
607 at tropical storm strength, and at hurricane strength.

HIRAD Wind Speed	Sample size	Bias (m s^{-1})		RMSD (m s^{-1})		MAD (m s^{-1})	
< TS: $< 17.5 \text{ m s}^{-1}$	304	2.2	18%	4.5	36%	3.5	27%
TS: $17.5 - 33.0 \text{ m s}^{-1}$	279	0.8	3%	6.2	27%	4.7	21%
Hurricane: $> 33.0 \text{ m s}^{-1}$	53	3.2	7%	10.7	26%	7.2	18%

608

609

610 Table 4. As in Table 3, but excluding Post-Erika 30 August, TS Patricia 21 October, and three
611 dubious HIRAD-dropsonde matches in the eyes of Hurricanes Patricia and Joaquin.

HIRAD Wind Speed	Sample size	Bias (m s ⁻¹)		RMSD (m s ⁻¹)		MAD (m s ⁻¹)	
< TS: < 17.5 m s ⁻¹	235	1.7	14%	4.1	33%	3.2	25%
TS: 17.5 – 33.0 m s ⁻¹	248	-0.1	-1%	5.6	25%	4.3	19%
Hurricane: > 33.0 m s ⁻¹	47	0.3	0%	6.3	16%	4.8	12%

612

613

614 **FIGURE CAPTIONS**

615

616 Figure 1. Unfiltered, unsmoothed excess brightness temperatures at (a) 4.0, (b) 5.0, (c) 6.0, (d)
617 6.6 GHz for leg across Hurricane Patricia at 2001 UTC 23 Oct 2015. +/-60° swath is plotted.
618 Solid black lines mark +/- 50° swath width.

619

620 Figure 2. (a) Weights derived from scan-position dependent relative biases for the flight leg in
621 Fig. 1. (b) Percentage contribution to the smoothed, filtered excess brightness temperature by
622 neighboring pixels in each across-track scan, from the weights combined with the spatial
623 Gaussian filter. The off-nadir angle (top axis) is the same as incidence angle, when aircraft pitch
624 and roll are both zero.

625

626 Figure 3. HIRAD footprint size as a function of off-nadir angle, before and after smoothing. An
627 aircraft altitude of 20 km is assumed.

628

629 Figure 4. As in Figure 1, but smoothed, filtered excess brightness temperatures.

630

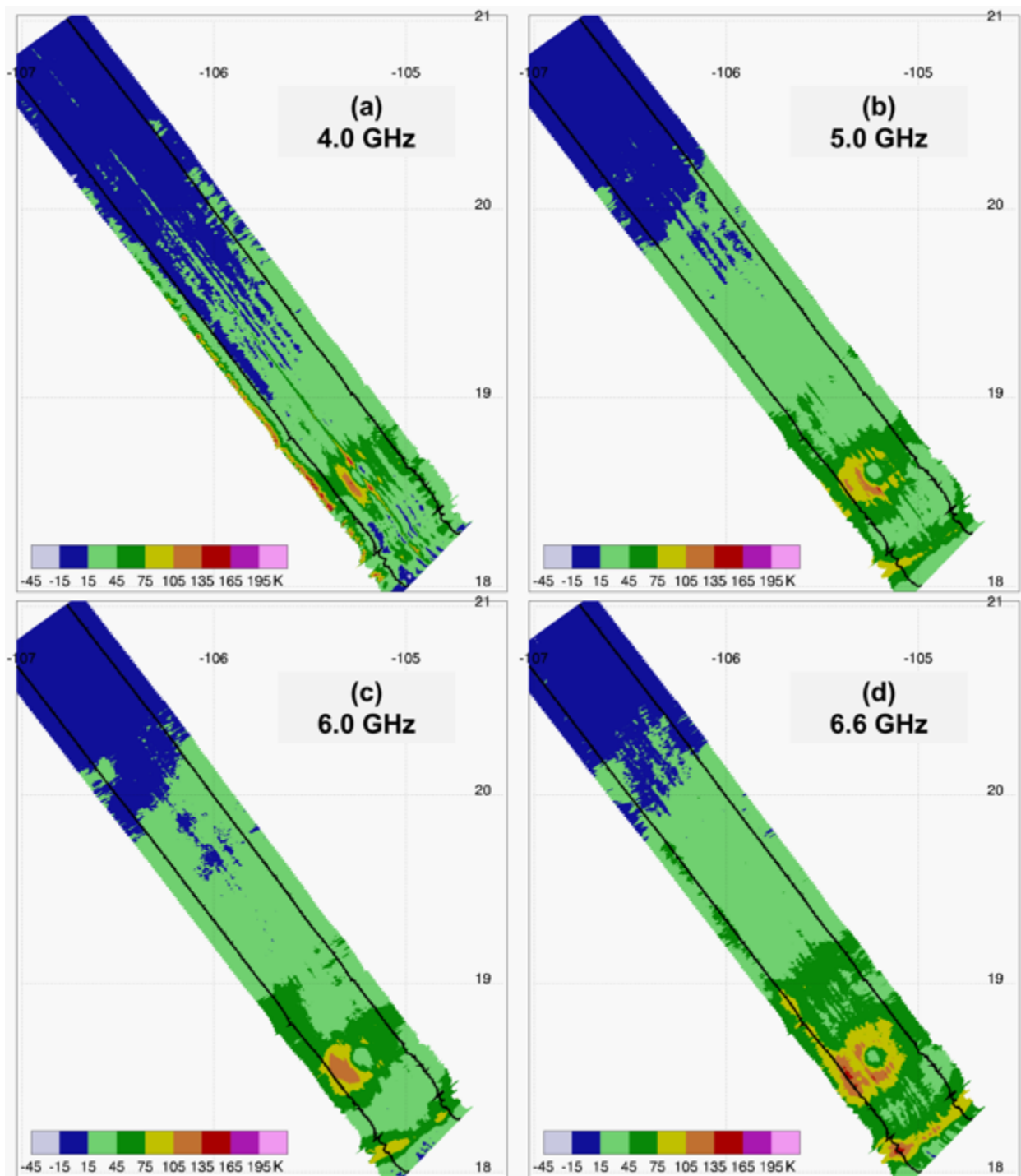
631 Figure 5. HIRAD retrieved surface wind speed versus dropsonde-estimated surface wind speed.
632 (a) Stratified by flight. (b) Stratified by HIRAD incidence angle. Solid lines mark +/-10%
633 agreement; dashed lines mark +/-20% agreement.

634

635 Figure 6. (a) HIRAD retrieved wind speeds (m s^{-1}) for the +/-50° swath across the eyewall of
636 Hurricane Patricia at 2001 UTC 23 Oct 2015. Printed numbers compare dropsonde (top

637 numbers) versus HIRAD (bottom numbers) wind speeds at the dropsonde locations. Two
638 dropsonde-HIRAD pairings discussed in the text are circled. Dropsonde trajectories and wind
639 barbs overlaid on the HIRAD wind speed are shown in Rogers et al. (2017). (b) Wind speed (+/-
640 60° swath) for all flight legs, 1946 – 2159 UTC. (c) Rain rate corresponding to (b). (d) AMSR-
641 2 89 GHz horizontal polarization brightness temperature at 2027 UTC, image courtesy Josh
642 Cossuth and the NRL Monterey TC web page team.

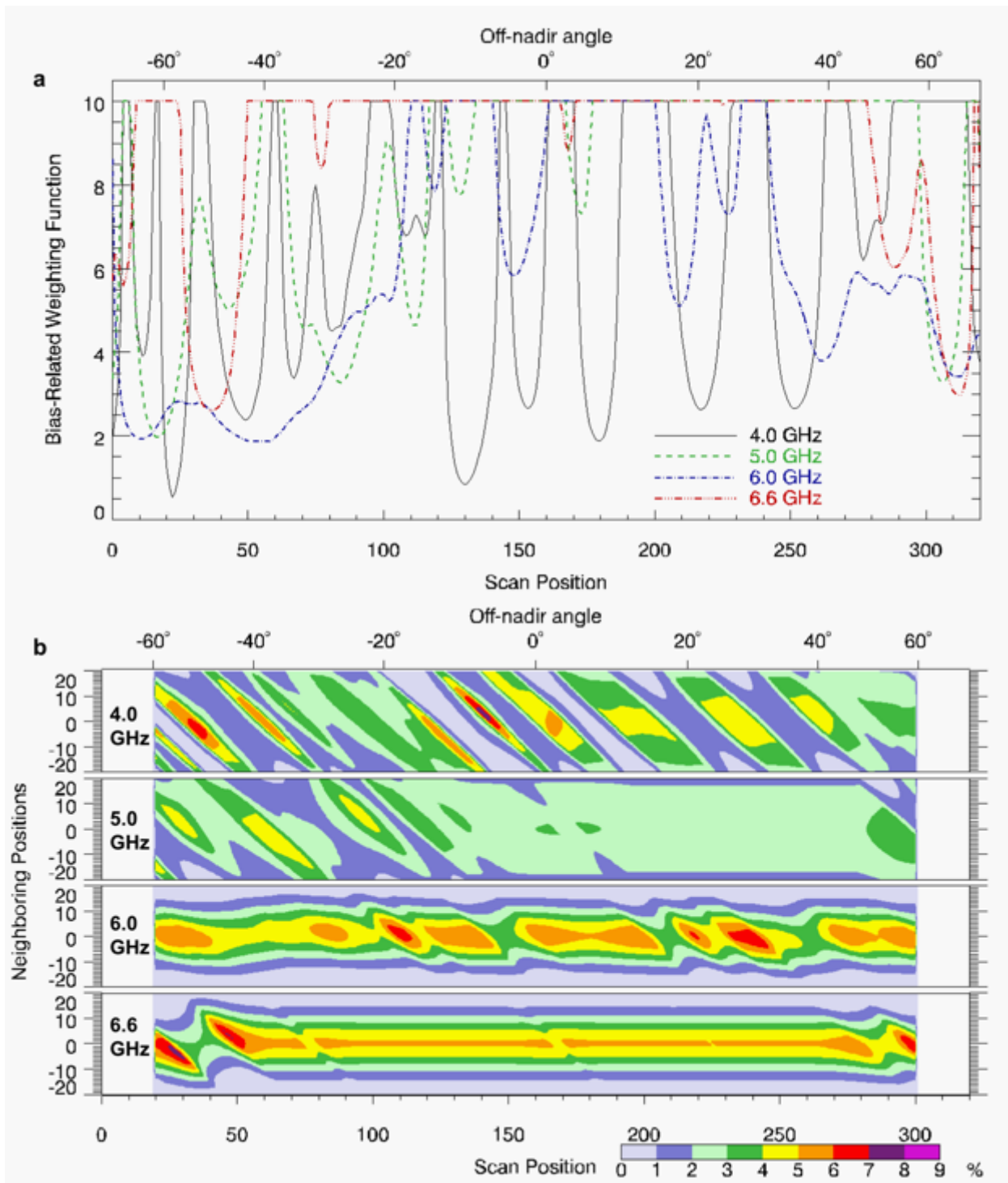
643
644 Figure 7. (a) Surface wind speed (m s^{-1}) for a 1-km resolution idealized numerical model, with a
645 hypothetical aircraft figure-4 pattern applied. (b) As in (a), but smoothed with HIRAD's antenna
646 pattern. (c) As in (a), but 10 minutes later to simulate conditions encountered by dropsondes.
647 (d) The difference (b) – (c).



648

649 Figure 1. Unfiltered, unsmoothed excess brightness temperatures at (a) 4.0, (b) 5.0, (c) 6.0, (d)
 650 6.6 GHz for leg across Hurricane Patricia at 2001 UTC 23 Oct 2015. +/-60° swath is plotted.
 651 Solid black lines mark +/- 50° width.

652

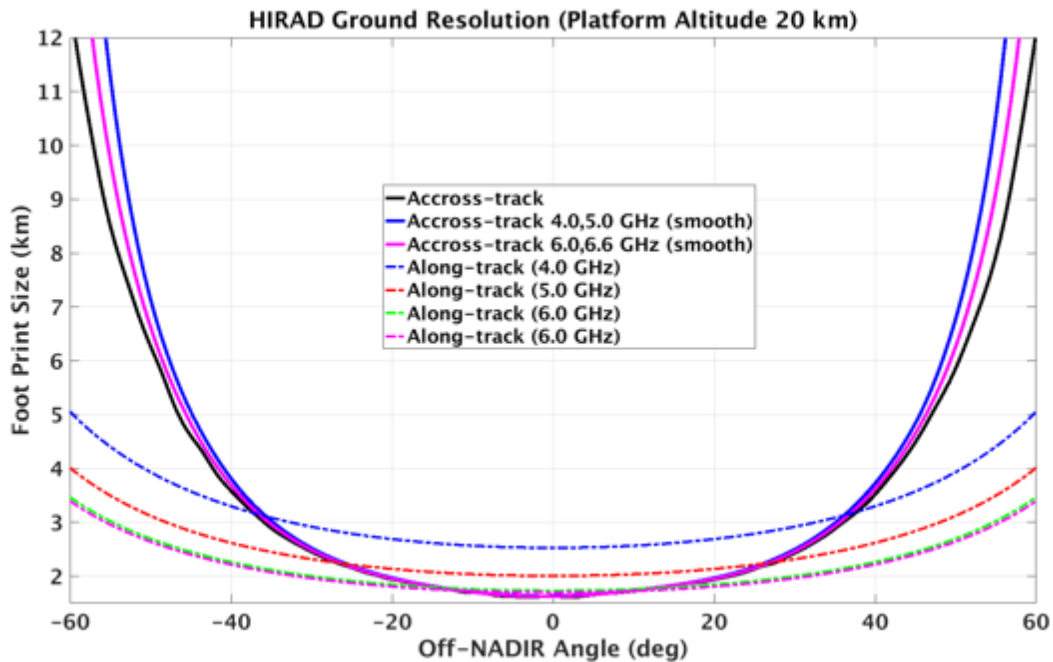


653

654 Figure 2. (a) Weights derived from scan-position dependent relative biases for the flight leg in
 655 Fig. 1. (b) Percentage contribution to the smoothed, filtered excess brightness temperature by
 656 neighboring pixels in each across-track scan, from the weights combined with the spatial

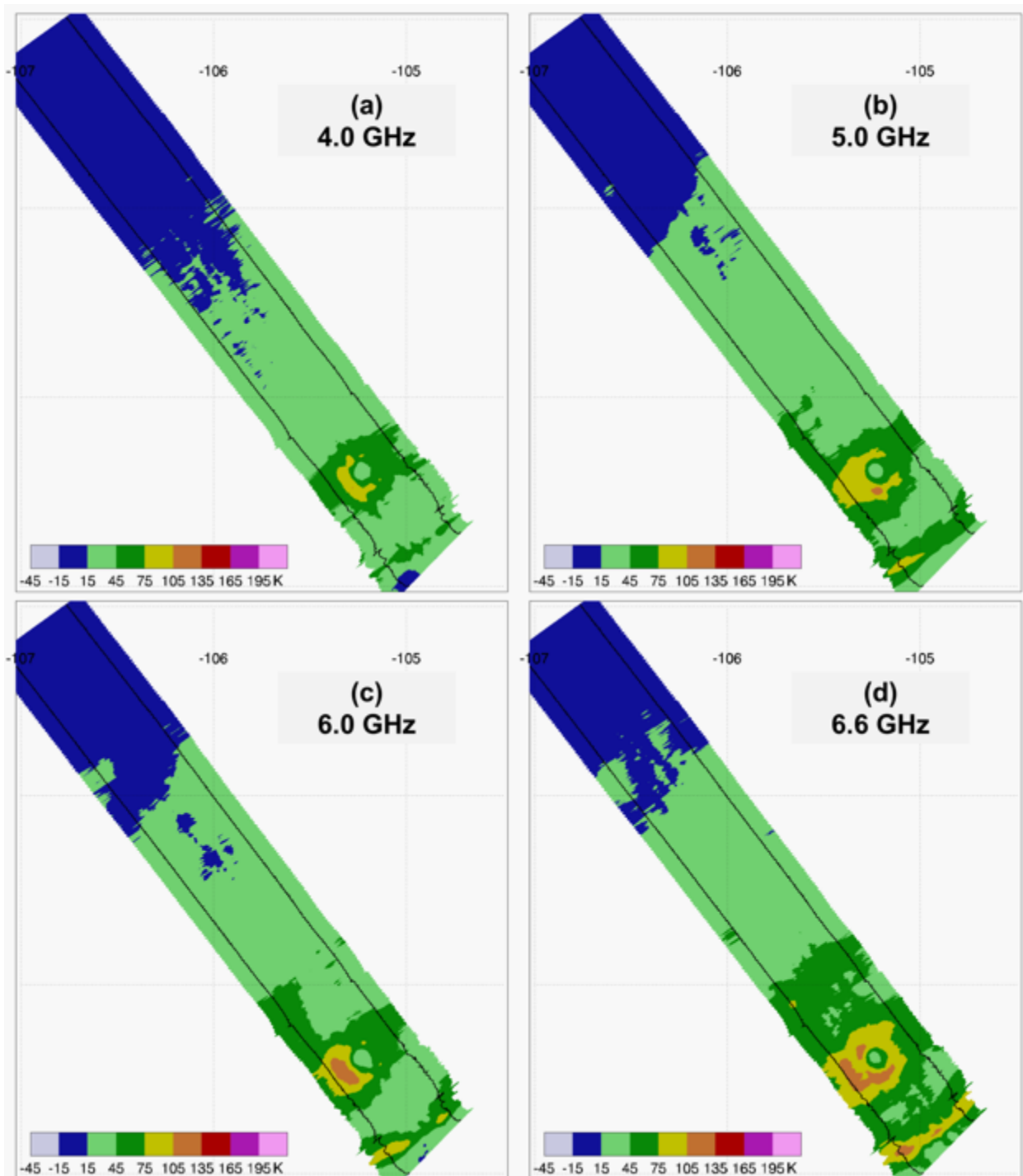
657 Gaussian filter. The off-nadir angle (top axis) is the same as incidence angle, when aircraft pitch
658 and roll are both zero.

659



660

661 Figure 3. HIRAD footprint size as a function of off-nadir angle, before and after smoothing. An
662 aircraft altitude of 20 km is assumed.



663

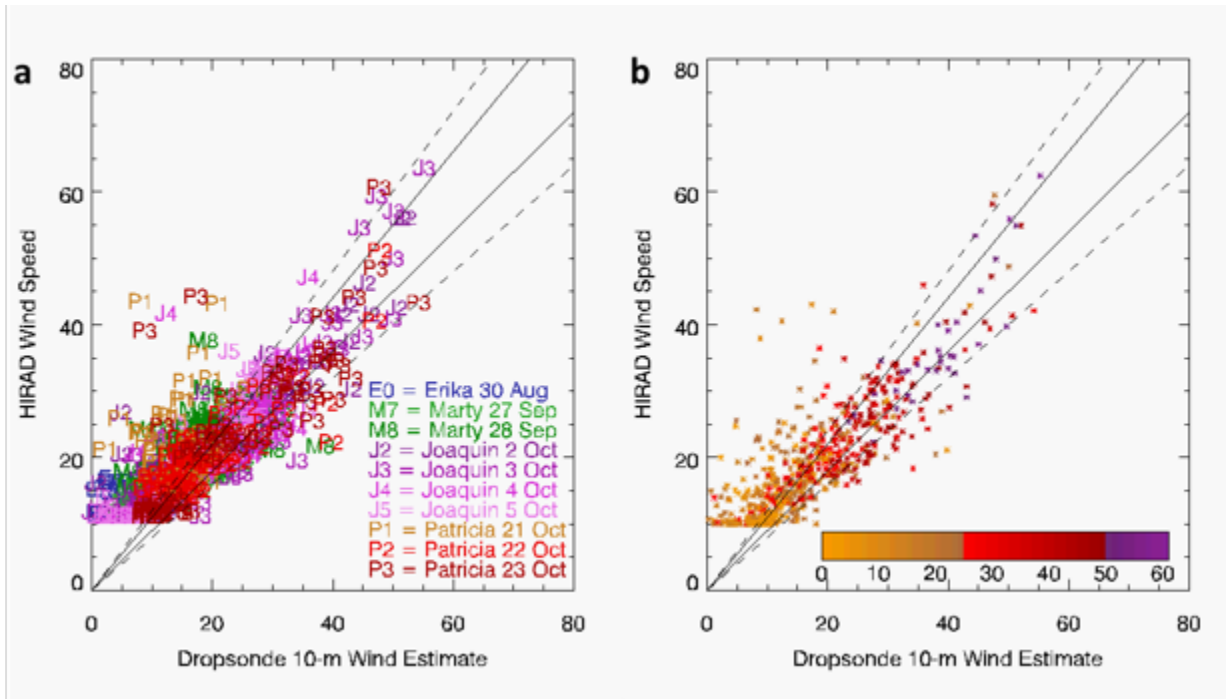
664 Figure 4. As in Figure 1, but smoothed, filtered excess brightness temperatures.

665

666

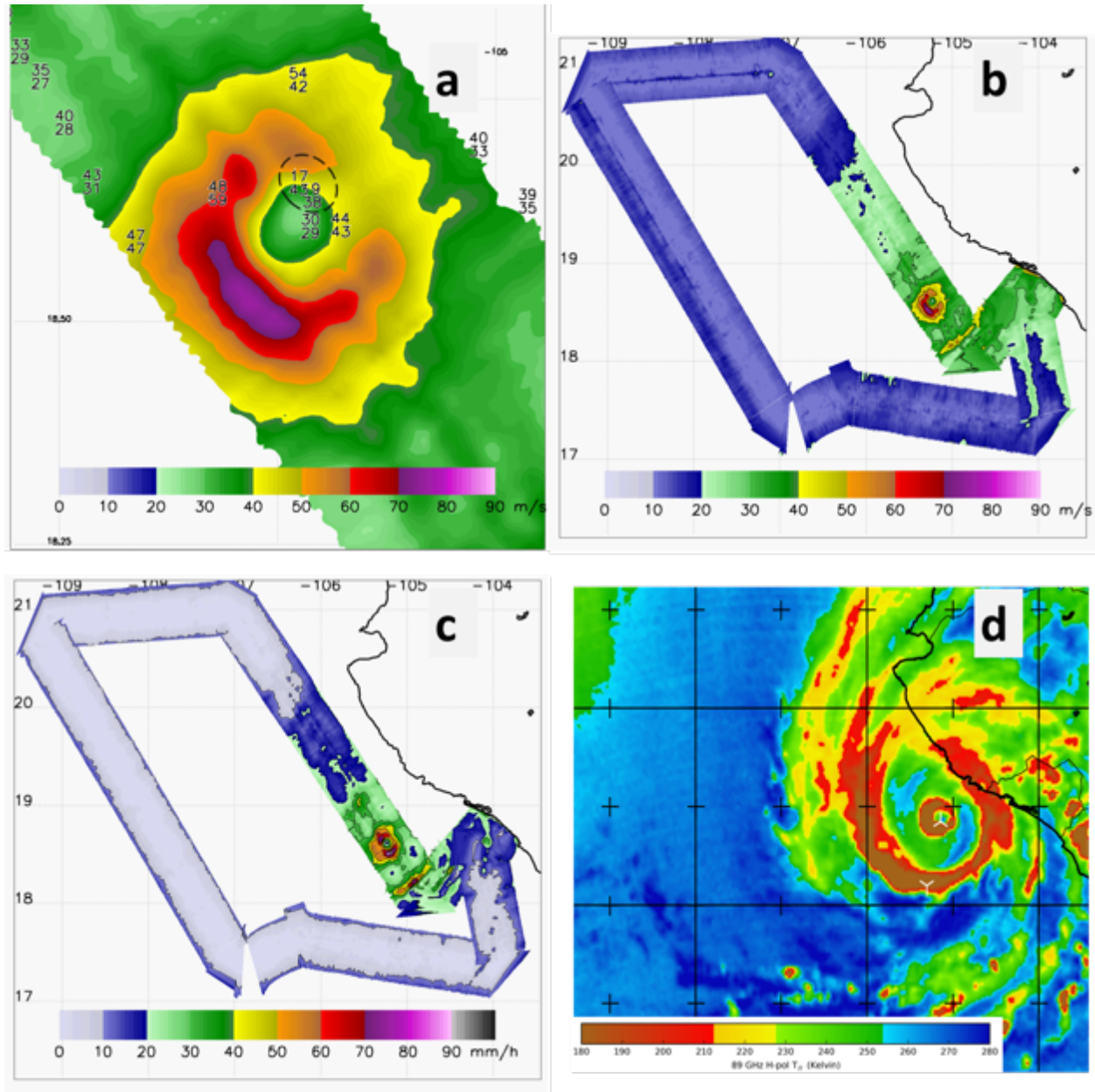
667

668
669



670
671
672
673

Figure 5. HIRAD retrieved surface wind speed versus dropsonde-estimated surface wind speed.
(a) Stratified by flight. (b) Stratified by HIRAD incidence angle. Solid lines mark +/-10%
agreement; dashed lines mark +/-20% agreement.



674

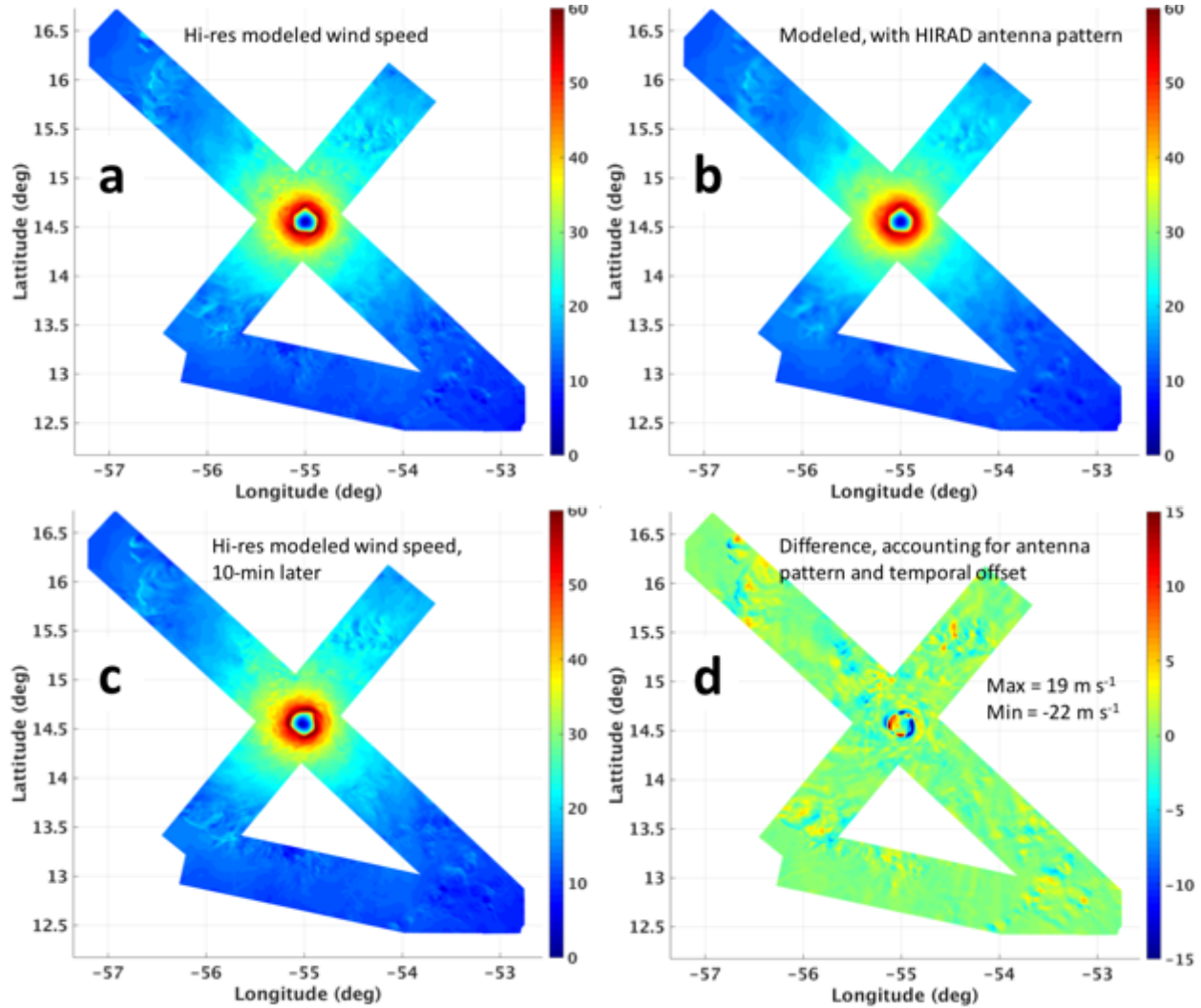
675 Figure 6. (a) HIRAD retrieved wind speeds (m s^{-1}) for the $\pm 50^\circ$ swath across the eyewall of
 676 Hurricane Patricia at 2001 UTC 23 Oct 2015. Printed numbers compare dropsonde (top
 677 numbers) versus HIRAD (bottom numbers) wind speeds at the dropsonde locations. Two
 678 dropsonde-HIRAD pairings discussed in the text are circled. Dropsonde trajectories and wind
 679 bars overlaid on the HIRAD wind speed are shown in Rogers et al. (2017). (b) Wind speed (\pm
 680 60° swath) for all flight legs, 1946 – 2159 UTC. (c) Rain rate corresponding to (b). (d) AMSR-

681 2 89 GHz horizontal polarization brightness temperature at 2027 UTC, image courtesy Josh

682 Cossuth and the NRL Monterey TC web page team.

683

684



685

686 Figure 7. (a) Surface wind speed (m s^{-1}) for a 1-km resolution idealized numerical model, with a
 687 hypothetical aircraft figure-4 pattern applied. (b) As in (a), but smoothed with HIRAD's antenna
 688 pattern. (c) As in (a), but 10 minutes later to simulate conditions encountered by dropsondes.
 689 (d) The difference (b) – (c).